Nanoscale Horizons

ROYAL SOCIETY OF CHEMISTRY

COMMUNICATION

View Article Online
View Journal | View Issue

Cite this: *Nanoscale Horiz.*, 2026, 11, 817

Received 8th September 2025,
Accepted 25th November 2025

DOI: 10.1039/d5nh00627a

rsc.li/nanoscale-horizons

MoS_2/Au–Ag@PEG nanosheets with plasmonic coupling effect-enhanced NIR-II photothermal therapy and silver ion release for combined treatment of MRSA infection

Qi Zhang,[a] Wen Li,[a] Songyirui Qiu,[a] Hongbin Gong,[a] Wenqing He,[a] Zhaowei Yin,[b] Lihui Yuwen *[a] and Lianhui Wang *[a]

The evolution of bacterial resistance to antibiotics has resulted in a global public health crisis, necessitating the development of novel antibiotic-independent antimicrobial strategies. In this study, MoS_2/Au–Ag@PEG nanosheets (MAAP NSs) were prepared *via* sequential deposition of gold and silver nanoparticles onto MoS_2 nanosheets (MoS_2 NSs), which were then used for the treatment of methicillin-resistant *Staphylococcus aureus* (MRSA) infections. Compared to MoS_2 NSs, MAAP NSs exhibit a significantly enhanced near-infrared region II (NIR-II) absorption at 1064 nm (a 7.51-fold increase), and the photothermal conversion efficiency improves by 50.7%, reaching 19.9%. Theoretical simulations reveal that the plasmonic coupling effect between adjacent Au–Ag nanoparticles (Au–Ag NPs) on the surface of MAAP NSs leads to the formation of hot spots and significantly enhances NIR-II light absorption, thereby improving the NIR-II photothermal performance. Moreover, the release of silver ions (Ag^+) can be effectively controlled by NIR laser irradiation. *In vitro* experimental results show that, upon NIR-II laser (1064 nm) exposure, MAAP NSs can effectively eliminate established MRSA biofilms with a bacterial inactivation efficiency of 99.992%. Notably, benefiting from the superior tissue penetration of the NIR-II laser, MAAP NSs exhibit potent therapeutic efficacy against both superficial wound infection and subcutaneous implant-associated MRSA biofilm infection in mouse models. *In vivo* results demonstrate that, under NIR-II laser stimulation, MAAP NSs can not only effectively kill 99.95% of MRSA in infected wounds and accelerate wound healing, but also remove MRSA biofilms from subcutaneous implant surfaces, achieving a 99.92% bacterial reduction. This work presents a novel strategy for designing NIR-II responsive antibacterial nanoagents based on plasmonic coupling effects in two-dimensional (2D) nanosheets and provides a promising solution for the treatment of antibiotic-resistant bacterial infections.

New concepts

This study introduces a novel strategy for the efficient fabrication of multifunctional antibacterial nanoagents responsive to near-infrared region II (NIR-II) light. The strategy involves the controlled growth of Au–Ag nanoparticles on the surface of two-dimensional (2D) MoS_2 nanosheets (MoS_2 NSs) to form MoS_2/Au–Ag@PEG nanosheets (MAAP NSs), which enables the modulation of the plasmonic coupling between noble metal nanoparticles, thereby enhancing the NIR-II photothermal properties. Additionally, this strategy facilitates the controlled release of silver ions (Ag^+) from MAAP NSs upon NIR-II laser irradiation. Unlike conventional antibacterial materials, MAAP NSs exhibit both excellent NIR-II photothermal performance and controlled Ag^+ release capability, resulting in remarkable synergistic antibacterial effects against both planktonic and biofilm-embedded bacteria *in vitro*. Owing to the superior tissue penetration of NIR-II light, MAAP NSs demonstrate excellent therapeutic efficacy against bacterial infections in both wound and implant infection mouse models. Given the simplicity and efficacy of the approach, along with the excellent antibacterial performance, we believe that it will provide significant guidance for the design and development of other highly effective antibacterial nanosystems, potentially contributing to the global fight against antibiotic resistance.

1. Introduction

Antimicrobial resistance (AMR) is recognized as one of the top ten global public health threats, responsible for an estimated 1.27 million deaths each year and substantial economic losses.[1,2] The World Bank projects that by 2050, AMR could result in costs of up to $100 trillion.[3] Excessive antibiotic use is a primary driver of resistant pathogens.[4–6] Accordingly, there is an urgent need for novel, antibiotic-independent antimicrobial strategies to address this challenge.

Photothermal therapy (PTT), characterized by spatiotemporal controllability and non-invasiveness, has emerged as a promising alternative to antibiotic therapy that has garnered

[a] State Key Laboratory of Flexible Electronics (LoFE) & Jiangsu Key Laboratory of Smart Biomaterials and Theranostic Technology, Institute of Advanced Materials (IAM), Nanjing University of Posts and Telecommunications, 9 Wenyuan Road, Nanjing 210023, China. E-mail: iamlhyuwen@njupt.edu.cn, iamlhwang@njupt.edu.cn
[b] Department of Orthopaedics, Nanjing First Hospital, Nanjing Medical University, Nanjing 210006, China

considerable attention. PTT involves the activation of photothermal agents (PTAs) by near-infrared (NIR) light, generating localized hyperthermia to inactivate bacteria.[7] However, PTT alone often requires elevated temperatures, which may induce inflammation and thermal injury to surrounding healthy tissues.[8,9] To mitigate these limitations, PTT is often combined with other therapeutic modalities, including antibiotic therapy, photodynamic therapy (PDT), chemodynamic therapy (CDT), and metal ion therapy.[10–14] Silver nanoparticles (Ag NPs), as classic antimicrobial agents, exert broad-spectrum antimicrobial activity through the release of silver ions (Ag^+), which can disrupt bacterial membranes, impair energy metabolism, damage DNA and protein synthesis, and induce oxidative stress, ultimately inhibiting bacterial proliferation.[15–18] They have been extensively utilized in biomedicine, personal care products, and industrial applications.[19–21] However, their small size and high surface area often lead to aggregation in complex physiological environments, impeding Ag^+ release and diminishing antibacterial efficacy.[22,23] Integrating PTT with Ag NPs not only facilitates Ag^+ release but also lowers the temperature threshold required for bacterial eradication, constituting an effective combined antimicrobial approach.[24–30] For example, Yue *et al.* modified Fe_3O_4 surfaces with polydopamine and loaded Ag NPs, achieving PTT/Ag^+/catalysis tri-modal synergistic therapy under 808 nm laser irradiation, significantly enhancing the treatment of MRSA infection.[31] He *et al.* developed a MoS_2/Ag/ICG composite system that activated Ag^+/PTT/PDT synergism under 808 nm laser irradiation, achieving 99.99% reduction in *Staphylococcus aureus*.[32] Despite promising therapeutic outcomes, most current PTT-Ag^+ combined strategies utilize near-infrared region I (NIR-I, 700–900 nm) lasers, which suffer from limited tissue penetration (~3 mm) and a low maximum permissible exposure (MPE) of 0.33 W cm^{-2}, restricting their applicability in complex physiological environments.[33] In contrast, near-infrared region II (NIR-II, 1000–1700 nm) lasers provide deeper tissue penetration (>10 mm) and a higher MPE (1.0 W cm^{-2}), offering greater potential for clinical application.[34,35] Although anisotropic gold nanostructures (*e.g.*, nanostars and nanorods) exhibit strong NIR-II responsiveness, their complex synthesis protocols hinder large-scale applications.[36–38] Research has shown that tuning the plasmonic coupling between noble metal nanoparticles can effectively enhance their absorption in the NIR-II region.[39–41] In this context, MoS_2 nanosheets (MoS_2 NSs), due to their high surface area and excellent photothermal properties, may serve as an ideal platform for the development of NIR-II responsive PTAs.[42]

In this study, MoS_2/Au–Ag@PEG nanosheets (MAAP NSs) were prepared by sequentially depositing gold and silver nanoparticles onto MoS_2 NSs, followed by functionalization with thiolated polyethylene glycol (PEG-SH) (Scheme 1a). By leveraging the plasmonic coupling of gold–silver nanoparticles (Au–Ag NPs), the engineered MAAP NSs enable NIR-II laser-activated combined photothermal and Ag^+ antibacterial therapy against MRSA infections (Scheme 1b). *In vitro* and *in vivo* experiments confirm that, under NIR-II laser irradiation, MAAP NSs can not only effectively inactivate both planktonic bacteria and biofilm-embedded bacteria, but also significantly promote wound healing and eradicate biofilms from subcutaneous implants. This study provides a promising design paradigm for the development of efficient NIR-II responsive nanoplatforms with antibacterial activity.

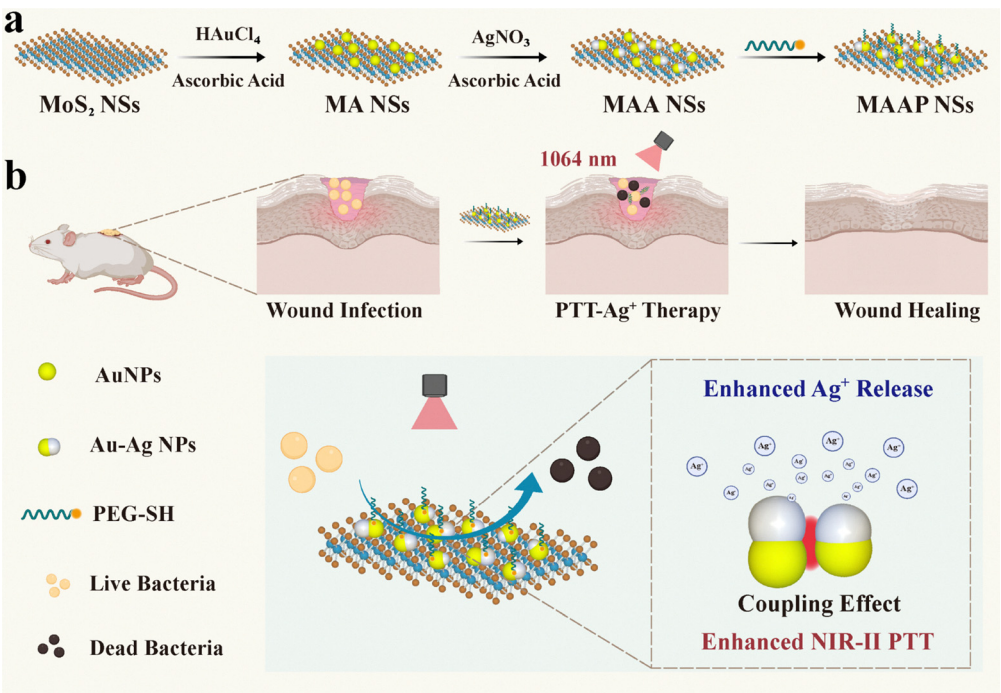

Scheme 1 (a) Schematic illustration of the preparation of MoS_2/Au–Ag@PEG nanosheets (MAAP NSs). (b) Combined treatment of MRSA infections *via* NIR-II photothermal therapy (PTT) and silver ions (Ag^+) release.

2. Experimental section

2.1 Preparation of MoS_2/Au nanosheets (MA NSs)

An aqueous MoS_2 NSs dispersion (50 μg mL^{-1}, 10 mL) was mixed with 1.25 mL of 200 mM ascorbic acid (AA) in a 20 mL sample vial equipped with a magnetic stir bar. The mixture was stirred at 1200 rpm for 5 min to ensure homogeneity. Subsequently, an aqueous solution of 2 mM $HAuCl_4{\cdot}3H_2O$ was added dropwise using a micro-injection pump (LSP02-2A, Longer Pump, China). Following the addition, the mixture was stirred for an additional 5 min to ensure a complete reaction. The resulting solution was then centrifuged at 10 000 rpm for 5 min, and the supernatant was discarded. The precipitate was redispersed in ultrapure water, sonicated, and subjected to two additional rounds of centrifugation to remove residual reactants. Finally, the purified precipitate was redispersed in ultrapure water to obtain an aqueous dispersion of MoS_2/Au nanosheets (MA NSs).

2.2 Preparation of MoS_2/Au–Ag nanosheets (MAA NSs)

Following a procedure similar to that described in Section 2.1, 10 mL of an aqueous MA NS dispersion (containing 50 μg mL^{-1} MoS_2) was mixed with 1.25 mL of 200 mM AA. After initial stirring, an aqueous solution of 1 mM $AgNO_3$ was added dropwise using the same micro-injection pump. The mixture was stirred for an additional 5 min. The product was centrifuged at 10 000 rpm for 5 min, and the supernatant was discarded. The precipitate was washed twice with ultrapure water *via* centrifugation and redispersed to yield MoS_2/Au–Ag nanosheets (MAA NSs).

2.3 Preparation of MoS_2/Au@PEG nanosheets (MAP NSs) and MoS_2/Au–Ag@PEG nanosheets (MAAP NSs)

To prepare MAP NSs and MAAP NSs, 5 mg of thiolated polyethylene glycol (PEG-SH) powder was added to 10 mL aqueous dispersions of either MA NSs or MAA NSs (each containing 50 μg mL^{-1} MoS_2). The mixture was stirred at 1200 rpm for 12 h at room temperature. Afterward, the solution was centrifuged at 12 000 rpm for 10 min, and the supernatant was discarded. The precipitate was redispersed in ultrapure water, sonicated, and washed with two additional rounds of centrifugation under the same conditions. The final dispersion of MAP NSs or MAAP NSs was obtained by redispersing the precipitate in ultrapure water.

2.4 Photothermal performance evaluation

Aqueous dispersions of the Au@PEG NPs + Ag@PEG NP mixture, the Au@PEG NPs + Ag@PEG NPs + MoS_2@PEG NS mixture, MoS_2@PEG NPs, MAP NSs, and MAAP NSs were prepared, with the concentrations adjusted to 20 μg mL^{-1} for MoS_2, 105 μg mL^{-1} for Au, and 61 μg mL^{-1} for Ag. Each dispersion was irradiated with a 1064 nm laser (MIL-N-1064, CNI, China) at a power density of 1.0 W cm^{-2} for 5 min. The temperature variations during irradiation were monitored and recorded using a Fortic225 near-infrared thermographic camera.

2.5 Finite-difference time-domain (FDTD) simulation

In this study, the finite-difference time-domain (FDTD) method was employed to simulate the local electric field intensity distribution of the following nanostructures: monodisperse gold nanoparticles (Au NPs), Au NP dimers, Au NPs on MAP NSs, and gold–silver nanoparticles (Au–Ag NPs) on MAAP NSs. The structural parameters were set as follows: monodisperse Au NPs with a diameter of 4.95 nm; Au NP dimers with a particle diameter of 4.95 nm and an interparticle distance of 15.00 nm; Au NPs on MAP NSs with a diameter of 4.95 nm and an interparticle distance of 2.75 nm; Au–Ag NPs on MAAP NSs, modeled as 4.95 nm Au cores coated with 0.925 nm Ag shells (corresponding to an overall diameter of ~6.80 nm) and separated by an interparticle distance of ~1.13 nm, according to TEM statistical analysis. All simulations were conducted using the Lumerical FDTD Solutions 2020 R2.4 software package. To evaluate the electromagnetic response of the nanostructures, the hot spot region between nanoparticles was analyzed based on the normalized electric field intensity (E), defined by the following equation:

$$E = \frac{E_l}{E_0}$$

where E_l represents the local electric field intensity at a specific point, and E_0 denotes the incident electric field intensity. In the case where $E = 5$, this indicates a fivefold enhancement of the local electric field intensity relative to the incident field intensity.

2.6 Evaluation of silver ion (Ag^+) release from MAAP NSs under laser irradiation

A phosphate-buffered saline (PBS) dispersion of MAAP NSs at 20 μg mL^{-1} was irradiated with a 1064 nm laser (1.0 W cm^{-2}) for 0, 2, 4, 6, 8, and 10 min at specified intervals. After irradiation, the supernatant was collected *via* ultrafiltration, and the concentration of released Ag^+ was quantified using an inductively coupled plasma optical emission spectrometer (ICP-OES).

2.7 *In vitro* anti-biofilm effects

To evaluate the anti-biofilm efficacy of MAAP NSs, preformed MRSA biofilms grown in 96-well plates were gently washed and incubated with 200 μL of saline, MAP NSs (MoS_2: 20 μg mL^{-1}), or MAAP NSs (MoS_2: 20 μg mL^{-1}) at 37 °C for 6 h. In the laser treatment groups, samples were irradiated with a 1064 nm laser at a power density of 0.8 W cm^{-2} for 5 min. The treatment outcomes were assessed using the following methods:

For confocal laser scanning microscopy (CLSM) observation, the treated MRSA biofilms were stained with Calcein-AM for 20 min, followed by imaging using a laser confocal scanning microscope (FV1000MPE, IX81, Olympus) and three-dimensional (3D) reconstruction and biofilm thickness analysis was conducted using the FV10-ASW software.

For the quantitative assessment of viable MRSA within the biofilms after various treatments, bacteria from treated MRSA

biofilms were collected by ultrasonication and resuspended in 1 mL of saline. The resulting suspension was serially diluted and plated on agar for colony-forming unit (CFU) counting to determine viable bacterial numbers.

For morphological characterization, MRSA biofilms were cultivated on indium tin oxide (ITO) glass slides (1 cm^2). Following various treatments, biofilms were fixed with 2.5% glutaraldehyde for 30 min and subsequently dehydrated through a graded ethanol series (15%, 30%, 50%, 75%, and 100%) for 15 min each. After air-drying, the samples were sputter-coated with a ~2.5 nm gold layer for scanning electron microscopy (SEM) imaging.

For quantitative analysis of biofilm biomass, the treated MRSA biofilms were fixed with 4% paraformaldehyde for 10 min and stained with 0.02% crystal violet solution for 1 h. The samples were washed three times with saline and imaged using an inverted fluorescence microscope (Olympus IX71). Afterward, the absorbance at 590 nm was measured following dissolution of the crystal violet in 95% ethanol. The relative biofilm biomass was calculated using the following equation:

$$\text{Relative biofilm biomass (\%)} = \frac{A_{\text{MAAP}} - A_{\text{blank}}}{A_{\text{saline}} - A_{\text{blank}}} \times 100\%$$

where A_{saline}, A_{MAAP} and A_{blank} represent the absorbance values of the saline-treated group, the MAAP NSs-treated group, and the solvent and control wells, respectively.

2.8 *In vivo* treatment of wound infection

All animal experiments were conducted in accordance with the Guidelines for the Care and Use of Laboratory Animals from Nanjing Medical University and were approved by the Animal Ethics Committee of Nanjing Medical University. Female BALB/c mice (6–7 weeks old) were purchased from Jiangsu Qinglongshan Biotechnology Co., Ltd (Jiangsu, China).

To establish the wound infection model, a full-thickness circular wound with an 8 mm diameter was created on the dorsal side of each mouse. Subsequently, a 1.5 cm × 1.5 cm square film dressing (Tegaderm Film, 3 M) was applied to cover the wound area. Then, 50 μL of MRSA suspension (1.0×10^8 CFU per mL) prepared in LB broth containing 1% glucose was injected beneath the dressing using a syringe. The MRSA-infected wound model was established after a 48-hour incubation period. Female BALB/c mice with MRSA-infected wounds were then randomly divided into six groups (n = 3 per group): saline, NIR, MAP, MAP + NIR, MAAP, and MAAP + NIR. The mice in the MAP group and MAAP group were injected with 50 μL of MAP NS dispersion (MoS_2: 20 μg mL^{-1}) and MAAP NS dispersion (MoS_2: 20 μg mL^{-1}), respectively, on the wounds. The mice in the saline + NIR group, MAP + NIR group, and MAAP + NIR group were irradiated with a 1064 nm laser at a power density of 0.6 W cm^{-2} for 10 min. After treatment, wound photographs were taken every two days to monitor the healing process. On day 8 post-treatment, wound tissues were harvested for CFU quantification to evaluate the antibacterial efficacy of the treatment. For histological analysis, the infected tissues of the mice were fixed in 4% paraformaldehyde solution for 12 h and then processed according to standard protocols for hematoxylin and eosin (H&E) staining.

2.9 *In vivo* treatment of implant infection

To establish the implant infection model, medical titanium plates (5 mm in diameter) were incubated together with 1 mL of MRSA suspension (1.0×10^7 CFU per mL) in LB broth containing 1% glucose at 37 °C for 48 h to facilitate the formation of mature biofilms. The biofilm-coated titanium plates were then implanted subcutaneously into the mice, and the incisions were sutured. The MRSA biofilm-infected implant model was established one day post-implantation. Female BALB/c mice bearing MRSA biofilm-infected implants were then randomly assigned to four groups (n = 4 per group): saline, NIR, MAAP, and MAAP + NIR. Each mouse received a subcutaneous injection of 50 μL of saline or MAAP NSs (MoS_2: 20 μg mL^{-1}) near the implant site. For the laser treatment groups, the implant area was irradiated with a 1064 nm laser at a power density of 0.8 W cm^{-2} for 10 min. On day 8 post-treatment, the implants were harvested and subjected to crystal violet staining and CFU quantification to evaluate biofilm disruption and bacterial viability.

2.10 Statistical analysis

All data are expressed as the mean ± standard deviation (SD). Statistical analyses were performed using one-way analysis of variance (ANOVA) followed by Tukey's *post hoc* test. Differences were considered statistically significant at probability (p) < 0.05 ($^*p < 0.05$, $^{**}p < 0.01$, $^{***}p < 0.001$, and $^{****}p < 0.0001$).

3. Results and discussion

3.1 Preparation and characterization of MAAP NSs

MoS_2 NSs were prepared *via* an ultrasonication-assisted lithium intercalation method developed by our group.[43] The morphology of the obtained MoS_2 NSs was characterized using transmission electron microscopy (TEM) and high-resolution TEM (HRTEM). As depicted in Fig. 1a, the MoS_2 NSs exhibited a uniform morphology with an average size of approximately 124 nm. The HRTEM image of MoS_2 NSs (Fig. S1) reveals a well-defined crystal structure, with a lattice spacing of approximately 2.7 Å, corresponding to the (100) crystal plane of MoS_2 NSs, which is consistent with previous reports.[44] MoS_2/Au nanosheets (MA NSs) were prepared *via* the *in situ* growth of gold nanoparticles (Au NPs) on MoS_2 NSs using ascorbic acid as a reducing agent.[45] This process was further extended to include additional reduction and deposition of silver, resulting in MoS_2/Au–Ag nanosheets (MAA NSs). It is worth noting that pre-growth of Au NPs is indispensable for the successful fabrication of MAA NSs, as direct addition of the Ag^+ precursor to MoS_2 NSs led to extensive precipitation (Fig. S2). As illustrated in Fig. 1b, the MA NSs were uniformly decorated with Au NPs, with an average size of approximately 4.95 nm and an interparticle distance of 2.75 nm (Fig. S3). The successful formation of Au NPs is further confirmed by the observed

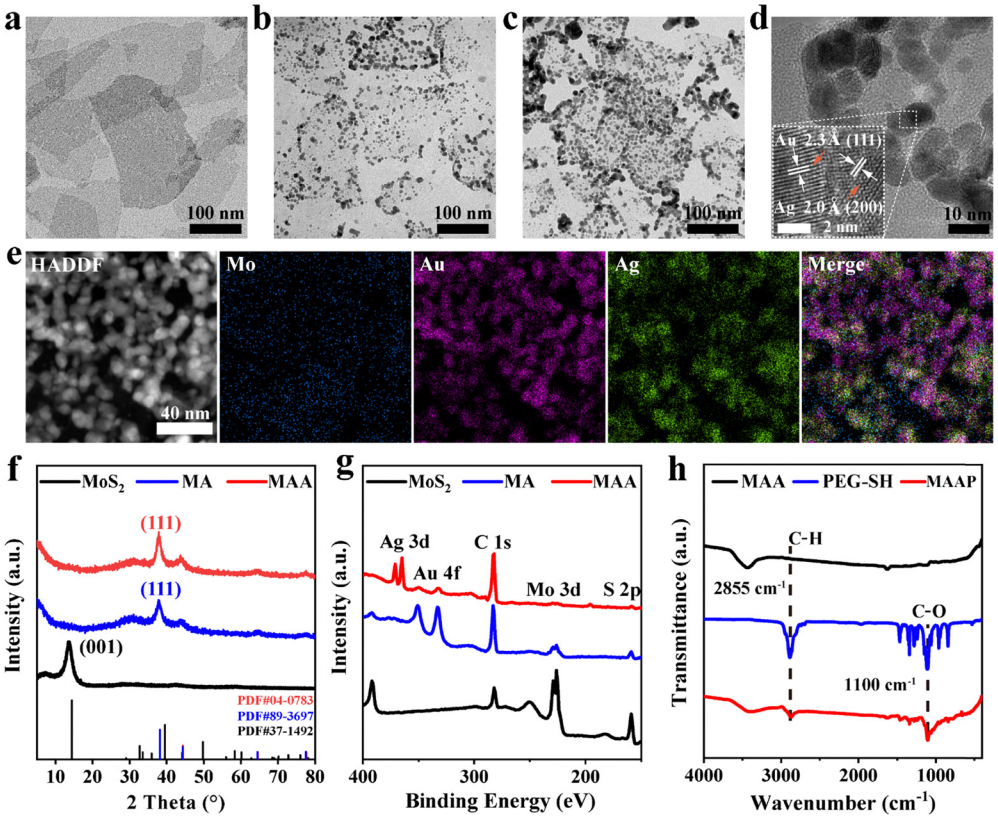

Fig. 1 Structural and compositional characterization of MoS_2 NSs, MA NSs, and MAA NSs. Transmission electron microscopy (TEM) images of (a) MoS_2 NSs, (b) MA NSs, and (c) MAA NSs. (d) High-resolution transmission electron microscopy (HRTEM) image of MAA NSs. (e) High-angle annular dark-field scanning transmission electron microscopy (HAADF-STEM) image of MAA NSs with corresponding energy-dispersive spectroscopy (EDS) elemental mapping of Mo, Au, and Ag. (f) X-ray diffraction (XRD) patterns of MoS_2 NSs, MA NSs, and MAA NSs. (g) X-ray photoelectron spectroscopy (XPS) spectra of MoS_2 NSs, MA NSs, and MAA NSs. (h) Fourier transform infrared (FT-IR) spectroscopy spectra of MAA NSs, PEG-SH, and MAAP NSs.

crystal lattice spacing of 2.3 Å, corresponding to the (111) plane of Au NPs (Fig. S4).[46] Fig. 1c presents densely packed Au–Ag nanoparticles (Au–Ag NPs) on MAA NSs, with an average size of approximately 6.82 nm and an interparticle distance of 1.13 nm (Fig. S5), while the corresponding HRTEM image (Fig. 1d) displays distinct Au–Ag crystal interfaces. Furthermore, high-angle annular darkfield scanning transmission electron microscopy (HAADF-STEM) was used to analyze the elemental distribution in MAA NSs. As shown in Fig. 1e, molybdenum (Mo), gold (Au), and silver (Ag) are homogeneously distributed throughout the MAA NSs. The crystal structure and elemental composition of MoS_2 NSs, MA NSs, and MAA NSs were characterized using X-ray diffraction (XRD) and X-ray photoelectron spectroscopy (XPS). As illustrated in Fig. 1f, the diffraction peak near 14° corresponds to the (001) plane of MoS_2 NSs (JCPDS no. 37-1492), consistent with previous reports.[47] Due to the growth of metal nanoparticles, the stacking of MoS_2 layers is disrupted, leading to the disappearance of the 14° diffraction peak in MA NSs and MAA NSs.[45] In the XRD pattern of MA NSs, the diffraction peak at 38.5° corresponds to the (111) plane of Au (JCPDS no. 89-3697), while in the XRD pattern of MAA NSs, the diffraction peak at 38.1° corresponds to the (111) plane of Ag (JCPDS no. 04-0783).[48,49] As shown in Fig. 1g, the XPS survey spectrum of MAA NSs exhibits distinct binding energy peaks corresponding to Au, Ag, Mo, and S. The binding energy peaks near 229.2 eV and 162.4 eV are attributed to Mo 3d and S 2p, respectively. Additionally, the binding energy peaks at 87.4 eV and 83.8 eV correspond to the Au $4f_{5/2}$ and $4f_{7/2}$ orbitals, while the peaks at 368.1 eV and 374.1 eV are assigned to Ag $3d_{5/2}$ and Ag $3d_{3/2}$, respectively (Fig. S6). The simultaneous presence of binding energy peaks for Mo, Au, and Ag in MAA NSs further confirms the successful growth of Au–Ag NPs on MoS_2 NSs.

To further improve the biocompatibility of MA NSs and MAA NSs for potential biomedical applications, their surfaces were functionalized with PEG-SH, resulting in the formation of MA@PEG NSs (MAP NSs) and MAA@PEG NSs (MAAP NSs), respectively. The Fourier-transform infrared (FT-IR) spectra (Fig. 1h) of MAAP NSs exhibit additional absorption peaks at 2855 cm^{-1} and 1100 cm^{-1} compared to MAA NSs, which correspond to the stretching vibrations of C–H bonds and C–O–C bonds in PEG-SH, confirming the successful surface modification.[50,51] As shown in Fig. S7 and S8, both MAP NSs and MAAP NSs are uniformly dispersed in PBS and cell medium and remain stable against aggregation, indicating that PEG-SH modification effectively enhances their colloidal stability.

3.2 Coupling effect-enhanced photothermal properties and silver ion release behavior of MAAP NSs

The optical properties of the aqueous dispersions of Ag@PEG NPs (AgP NPs), MoS_2@PEG NSs (MP NSs), Au@PEG NPs (AuP NPs), their mixture (AgP NPs + AuP NPs + MP NSs), MAP NSs, and MAAP NSs were evaluated using ultraviolet-visible-near infrared (UV-vis-NIR) absorption spectroscopy. The concentrations of the individual components were fixed as follows: 5 μg mL^{-1} for MoS_2, 26 μg mL^{-1} for Au, and 15 μg mL^{-1} for Ag in all formulations containing these components. As shown in Fig. 2a, AuP NPs, AgP NPs, MP NSs, and their mixture (AgP NPs + AuP NPs + MP NSs) exhibit limited absorption in the NIR-II region. In sharp contrast, MAP NSs and MAAP NSs display markedly enhanced absorbance from the ultraviolet to the NIR-II range, with absorbance at 1064 nm increased by 1.8- and 2.3-fold, respectively, compared with the mixed solution, highlighting the superior NIR-II absorbance of MAAP NSs.

The photothermal properties of MP NSs, binary mixtures (AgP NPs + AuP NPs), ternary mixtures (AgP NPs + AuP NPs + MP NSs), and MAP NSs and MAAP NSs were investigated by monitoring the temperature changes of their aqueous dispersions under NIR-II laser irradiation (1064 nm, 1.0 W cm^{-2}). As shown in Fig. 2b, after 5 min of NIR-II laser irradiation, the temperature of MP NSs, the ternary mixtures (AgP NPs + AuP NPs + MP NSs), MAP NSs, and MAAP NS aqueous dispersions (all containing 20 μg mL^{-1} MoS_2) increased by 15.8 °C, 19.7 °C, 34.3 °C, and 35.6 °C, respectively, while the temperature of the mixture of AuP NPs and AgP NPs increased by only 9.7 °C, demonstrating the superior photothermal performance of MAP NSs and MAAP NSs in the NIR-II range. Moreover, the photothermal stability of

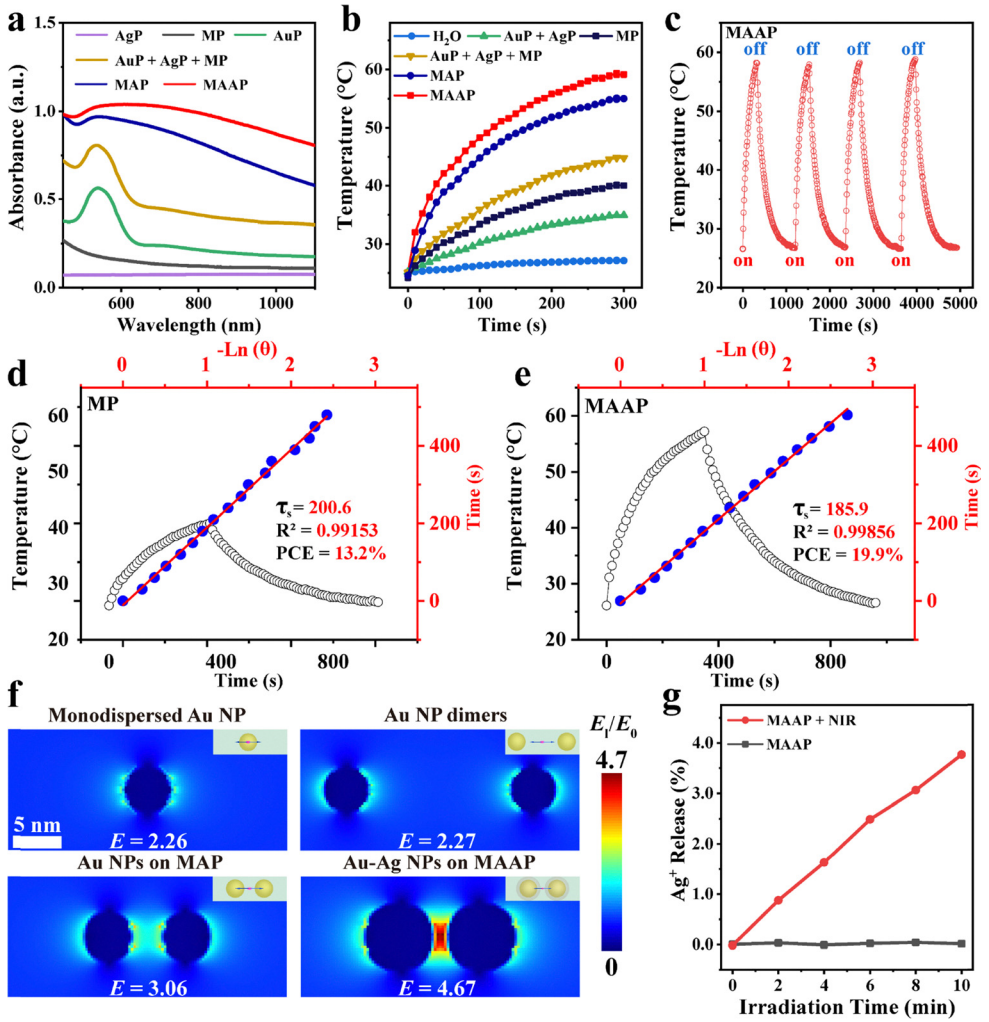

Fig. 2 Photothermal properties and silver ion release behavior of MAAP NSs. (a) UV-vis-NIR absorption spectra of AgP NPs, MP NSs, AuP NPs, their mixture (AgP NPs + AuP NPs + MP NSs), MAP NSs, and MAAP NS aqueous dispersions. (b) Photothermal heating curves of MP NSs, binary mixtures (AgP NPs + AuP NPs), ternary mixtures (AgP NPs + AuP NPs + MP NSs), and MAP NS and MAAP NS aqueous dispersions. (c) Temperature variation of MAAP NS aqueous dispersions over four cycles of on/off NIR-II laser irradiation. Calculation of photothermal conversion efficiency (PCE) for (d) MP NSs and (e) MAAP NSs, respectively. (f) Simulated electric field intensity distribution of monodisperse Au NP, Au NP dimers, Au NPs on MAP NSs, and Au–Ag NPs on MAAP NSs using finite-difference time-domain (FDTD) numerical simulations. The insets show the corresponding schematic models. (g) Ag^+ release profiles of MAAP NSs in PBS, with or without NIR-II laser irradiation. Samples were all irradiated with a 1064 nm laser at a power density of 1.0 W cm^{-2}.

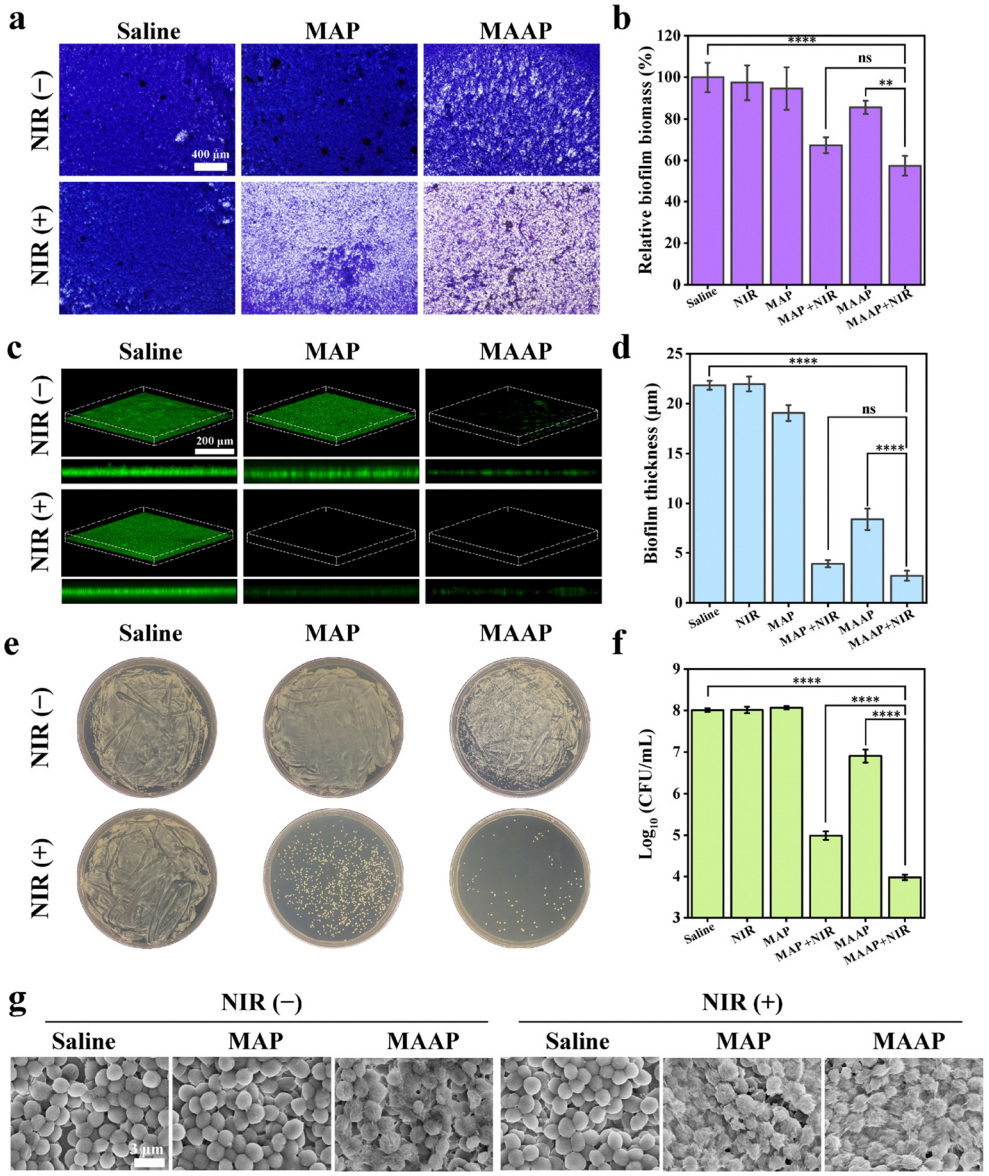

Fig. 3 *In vitro* antibiofilm activity of MAAP NSs. (a) Micrographs and (b) quantification of biofilm biomass in crystal violet-stained MRSA biofilms following different treatments. (c) 3D CLSM images of biofilms and (d) quantification of biofilm thickness following different treatments. (e) Representative images of MRSA colonies on agar plates and (f) corresponding CFU quantification after different treatments. (g) SEM images of MRSA biofilms following different treatments.

MAAP NSs was evaluated over four heating/cooling cycles, showing negligible performance degradation (Fig. 2c). Thermogravimetric analysis (TGA) results further demonstrated that MAAP NSs had minimal mass loss through a gradual temperature increase of up to 180 °C, revealing good thermal stability (Fig. S9). As shown in Fig. 2d and e, the photothermal conversion efficiency (PCE) of MAAP NSs at 1064 nm was calculated to be approximately 19.9%, significantly higher than that of MP NSs (13.2%). In addition, Table S1 provides a benchmark against previously reported NIR-II photothermal agents, showing that MAAP NSs exhibits a comparable PCE along with a higher mass extinction coefficient (MEC). To elucidate the underlying mechanism behind the enhanced photothermal effect of MAAP NSs, finite-difference time-domain (FDTD) numerical simulations were conducted, with a mesh-independence study performed beforehand to ensure the reliability of the results. As shown in Fig. S10, the calculated electric field distributions under different grid sizes (Δ) exhibited negligible discrepancies, and the hot spot locations and relative intensities remained consistent, confirming that the simulations are independent of mesh density. Because the surface electric field strength of metal NPs is positively correlated with their surface plasmon coupling effect, which significantly influences their extinction ability.[41,52] The simulations revealed that the hot spot regions, characterized by E, were located at the gaps between nanoparticles. The electric field intensity in the hot spot region of Au–Ag NPs on MAAP NSs reached up to 4.67 times that of the incident field, which is notably higher than the values observed in monodispersed Au

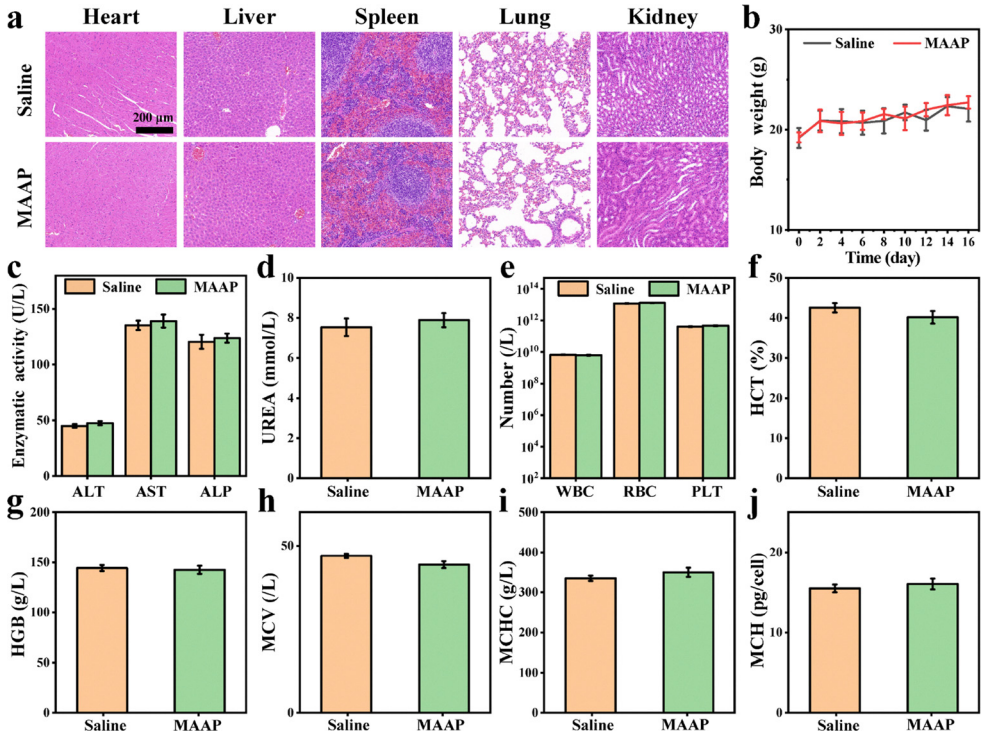

Fig. 4 *In vivo* toxicity evaluation of MAAP NSs in mice. (a) H&E-stained sections of major organs from mice on day 8 post-treatment with saline or MAAP NSs (MoS_2: 0.10 mg kg^{-1}, Au: 0.55 mg kg^{-1}, Ag: 0.32 mg kg^{-1}). (b) Weight curves of mice treated with saline or MAAP NSs. (c) Serum concentrations of alanine aminotransferase (ALT), aspartate aminotransferase (AST), and alkaline phosphatase (ALP). (d) Serum urea concentrations. (e) White blood cell (WBC), red blood cell (RBC), and platelet (PLT) counts. (f) Hematocrit (HCT), (g) hemoglobin (HGB), (h) mean corpuscular volume (MCV), (i) mean corpuscular hemoglobin concentration (MCHC), and (j) mean corpuscular hemoglobin (MCH) levels in blood on day 16 post-treatment.

NPs (2.26 times), Au NP dimers (2.27 times), and Au NPs on MAP NSs (3.06 times) (Fig. 2f). These results indicate that the superior photothermal effect of MAAP NSs likely arises from the enhanced electric field induced by strong interparticle coupling and the lightning rod effect of densely arranged Au–Ag NPs on the surface.

Considering the therapeutic relevance of Ag^+ release, we next investigated its release profile from MAAP NSs under different conditions. Ag^+ release was first evaluated at various temperatures (Fig. S11). At 25 °C, only ~0.6% of Ag^+ was released within 30 min, whereas at 37 °C the release increased to ~3.8%, and at 50 °C it further rose to ~7.4%. This temperature-dependent release is consistent with that in previous reports.[53] Additionally, we found that Ag^+ release is also influenced by pH. As shown in Fig. S12, 5.5% of Ag^+ was released under neutral conditions (pH 7.4, 45 °C), while 6.0% of Ag^+ was released under acidic conditions (pH 4.5, 45 °C). The dual-responsive Ag^+ release can improve the biological safety and therapeutic efficacy of MAAP NSs. Building on this result, we subsequently examined laser-triggered Ag^+ release. As shown in Fig. 2g, under 1064 nm irradiation (1.0 W cm^{-2}), MAAP NSs released ~3.8% of the total Ag^+ within 10 min, whereas negligible release was observed without irradiation. These results highlight the potential of MAAP NSs as dual-function therapeutic agents that combine NIR-II PTT with Ag^+ release. Moreover, the findings demonstrate that the enhanced release is primarily attributable to localized heating induced by their photothermal effect.

3.3 *In vitro* antibacterial activity of MAAP NSs

Given its propensity to cause various clinical infections, including bacteremia, infective endocarditis, and skin and soft tissue infections, MRSA was selected as the model bacterium in this study.[54] The antimicrobial capabilities of MAP NSs, MAAP NSs, the binary mixture (AuP NPs + AgP NPs), and the ternary mixture (AuP NPs + AgP NPs + MP NSs) were evaluated using the spread plate method. As depicted in Fig. S13, without NIR-II irradiation, MAP NSs exhibited negligible antibacterial activity. In contrast, MAAP NSs achieved a 1.9 log reduction (~98%) in MRSA viability. Similarly, the binary mixture (AuP NPs + AgP NPs) resulted in a 2.0 log reduction (~99%), while the ternary mixture (AuP NPs + AgP NPs + MP NSs) achieved a 1.9 log reduction (~98%), mainly owing to the intrinsic antibacterial effect of Ag^+. Under NIR-II laser irradiation, MAAP NSs demonstrated a remarkable 4.6 log reduction (~99.998%) in MRSA viability, which was substantially higher than that observed for MAP NSs (3.6 log, 99.97%), the ternary mixture of AuP NPs, AgP NPs, and MP NSs (3.0 log, 99.91%), and the binary mixture of AuP NPs, and AgP NPs (2.3 log, 99.5%). This superior antibacterial performance of MAAP NSs is attributed to the synergistic contribution of photothermal heating and Ag^+ release, both enhanced by plasmonic coupling between Au and Ag NPs.

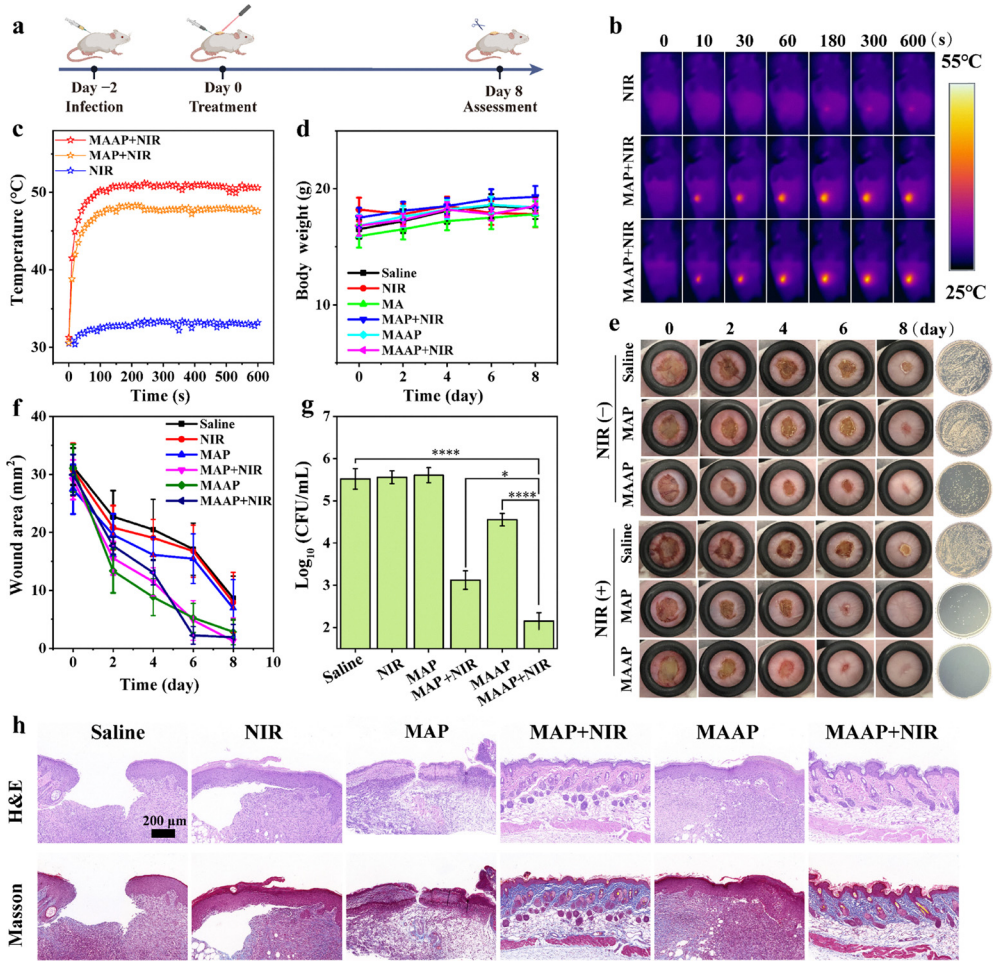

Fig. 5 Treatment of MRSA-infected wounds in mice using MAAP NSs. (a) Schematic illustration of the development of an *in vivo* MRSA-infected wound model and its subsequent treatment procedure. (b) Infrared thermal images of mice under NIR-II laser irradiation (1064 nm, 0.6 W cm^{-2}), along with (c) the corresponding photothermal heating curves. (d) Weight curves of mice subjected to different treatments. (e) Representative images of infected wounds under various treatments on days 0, 2, 4, 6, and 8 post-treatment. Corresponding images of MRSA colonies cultured from wound isolates on day 8 are also shown (rubber ring diameter: 8 mm). (f) Quantitative analysis of wound area reduction over time under different treatment conditions. (g) Quantification of bacterial CFU in infected wound tissues on day 8 post-treatment. (h) H&E and Masson's trichrome staining of infected wound tissues following different treatments.

3.4 *In vitro* antibiofilm effect of MAAP NSs

Due to the protective barrier formed by extracellular polymeric substances (EPSs), established biofilms are difficult to eradicate, necessitating the evaluation of MAAP NSs for preformed biofilm treatment.[55–57] To assess the antibiofilm effect of MAP NSs and MAAP NSs, MRSA biofilms were grown in 96-well plates. Biofilm disruption and antibacterial efficacy were assessed *via* crystal violet staining, fluorescence imaging, spread plate method, and SEM imaging.

As shown in Fig. 3a and b, the relative biomass of MRSA biofilms remained largely unchanged after treatment with MAP NSs alone, while MAAP NSs alone reduced the biomass to 85%. Upon exposure to NIR-II laser irradiation, the biofilm biomass decreased to 67% with MAP NSs and to 57% with MAAP NSs. Fluorescence imaging (Fig. 3c) further demonstrated reduced fluorescence intensity in the MAP + NIR, MAAP, and MAAP + NIR groups, indicating decreased bacterial viability. Correspondingly, the biofilm thickness decreased to 3.9 μm, 8.4 μm, and 2.7 μm in the MAP + NIR, MAAP, and MAAP + NIR groups, respectively, compared to 21.7 μm in the saline group (Fig. 3d). As illustrated in Fig. 3e and f, MAP NSs alone exhibited negligible antibacterial activity. Upon NIR-II laser irradiation, MAP NSs achieved a 3.2 log reduction (~99.94%) in bacterial viability, while MAAP NSs reached a 4.1 log reduction (~99.992%). SEM images (Fig. 3g) further demonstrated that MRSA maintained smooth, intact cell walls in the MAP group, but appeared distorted and wrinkled in the MAP + NIR, MAAP, and MAAP + NIR groups. These results demonstrate that MAAP NSs, by virtue of plasmonic coupling-enhanced NIR-II photothermal and Ag^+ release effects, can effectively disrupt the biofilm structure, reduce biomass and thickness, and eradicate embedded bacteria under NIR-II irradiation.

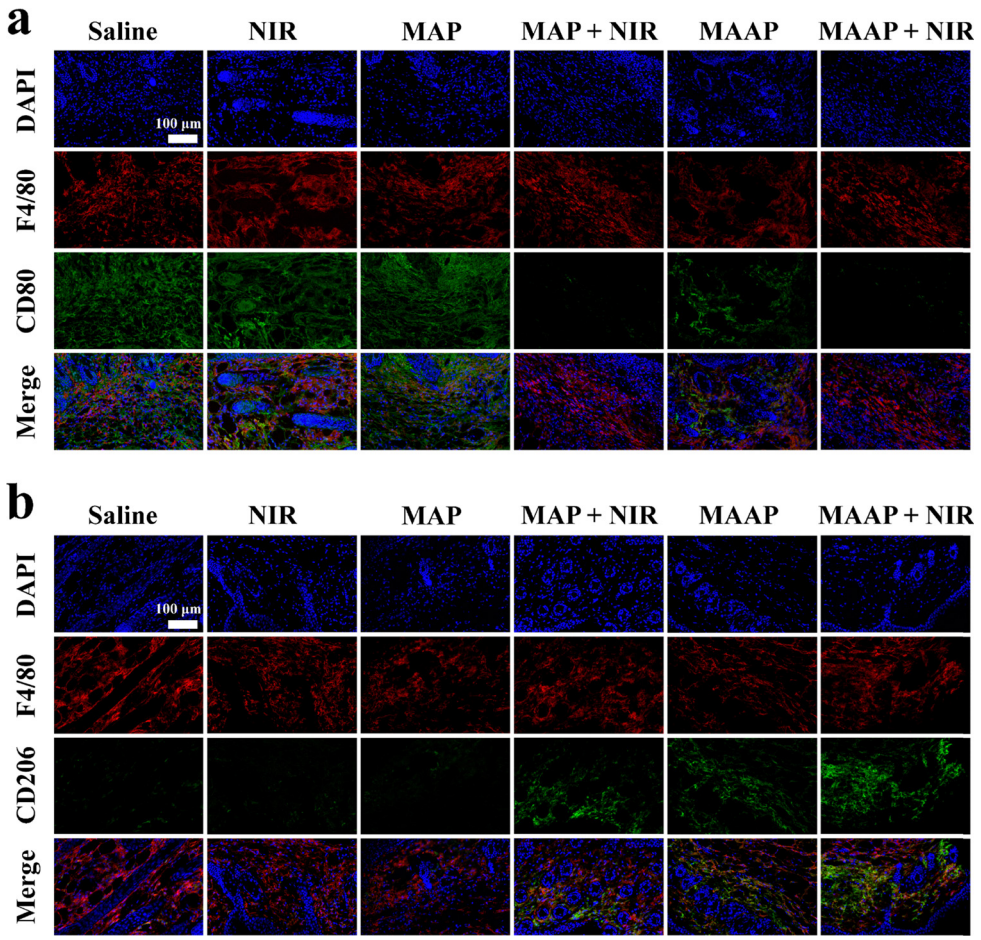

Fig. 6 Immunofluorescence staining of infected wound tissue sections from mice on day 8 post-treatment. (a) Representative images showing nuclei stained with DAPI (blue), macrophages labeled with F4/80 (red), and the M1 macrophage marker CD80 (green). (b) Representative images showing nuclei stained with DAPI (blue), macrophages labeled with F4/80 (red), and the M2 macrophage marker CD206 (green).

3.5 Biocompatibility evaluation of MAAP NSs

Before further applications, the biocompatibility of MAAP NSs was evaluated. Human liver cells (L-O2) and keratinocyte cells (HaCaT) were incubated with MAAP NS dispersions for 24 h, and cytotoxicity was assessed using the lactate dehydrogenase (LDH) assay. The viability of L-O2 cells and HaCaT cells remained above 85% and 91% after treatment with MAAP NSs at concentrations up to 40 μg mL^{-1} (Fig. S14a and b), indicating low cytotoxicity. The hemolytic effect of MAAP NSs was subsequently evaluated by incubating them with mouse red blood cells (RBCs). As shown in Fig. S14c, the supernatant remained nearly colorless, and the hemolysis ratio was below 5%, confirming the good hemocompatibility of MAAP NSs. Hematoxylin and eosin (H&E) staining was further employed to assess the *in vivo* biosafety of MAAP NSs. As shown in Fig. 4a, the H&E-stained sections of major organs from MAAP-treated mice exhibited no observable histopathological abnormalities compared to saline controls. Additionally, the body weights of MAAP-treated mice were not significantly different from those of healthy controls (Fig. 4b). Furthermore, blood biochemical and hematological analyses revealed no significant differences between MAAP-treated and healthy mice (Fig. 4c–j). These results collectively demonstrate that MAAP NSs exhibit excellent biocompatibility.

3.6 *In vivo* treatment of MRSA infections

In the MRSA-infected wound model, skin wounds were induced on the dorsal side of mice and subsequently treated (Fig. 5a). Infrared thermal images and temperature curves (Fig. 5b and c) revealed that, during NIR-II PTT (1064 nm, 0.6 W cm^{-2}, 10 min), wound temperatures rapidly increased to 47.6 °C in the MAP + NIR group and 50.2 °C in the MAAP + NIR group within 2 min, while the NIR-only group reached only 33.2 °C. Throughout the treatment period, mouse body weights remained within a reasonable range (Fig. 5d), suggesting good biocompatibility of MAAP NSs. By day 8 post-treatment (Fig. 5e), wound healing varied notably among groups, with significant MRSA reduction observed in the MAP + NIR, MAAP, and MAAP + NIR groups compared to saline groups. Wound area quantification (Fig. 5f) showed that wounds in the MAP + NIR, MAAP, and MAAP + NIR groups were reduced to 6.4%, 9.1%, and

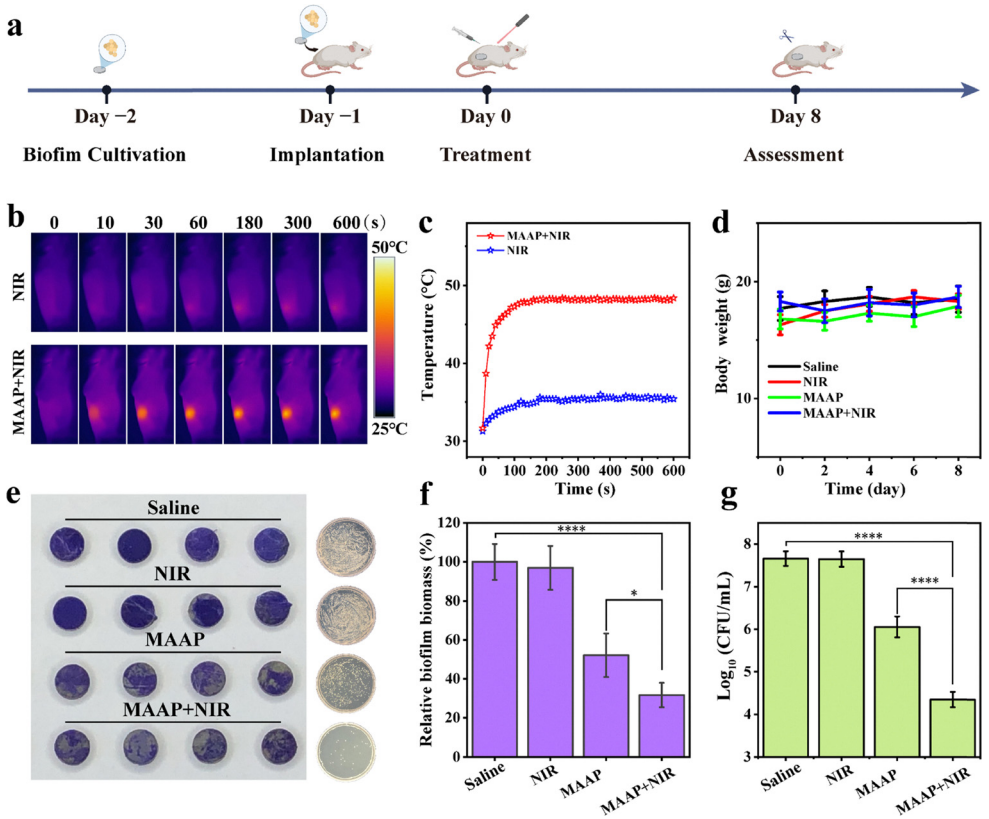

Fig. 7 Treatment of implant-associated MRSA biofilm infections in mice using MAAP NSs. (a) Schematic of the *in vivo* MRSA-infected implant model and treatment process. (b) Infrared thermal images and (c) corresponding temperature curves of mice under NIR-II laser irradiation (1064 nm, 0.8 W cm^{-2}). (d) Weight curves of mice following different treatments. (e) Images of crystal violet-stained infected implants. Corresponding images of MRSA colonies cultured from implant biofilms after different treatments are also shown. (f) Quantitative analysis of relative biofilm biomass after different treatments. (g) Bacterial CFU quantification on implant surfaces on day 8 post-treatment.

4.4% of their original size, respectively, whereas the saline group exhibited a wound closure of only 27.6% relative to the initial area. Bacterial inactivation efficiencies at the wound sites (Fig. 5g) were 2.4 log (99.6%) for MAP + NIR, 0.9 log (87%) for MAAP, and 3.3 log (99.95%) for MAAP + NIR, aligning well with the observed wound healing outcomes. These therapeutic outcomes were further validated by histological examinations. As shown in Fig. 5h, H&E staining images demonstrated relatively intact epidermal architecture in the MAP + NIR and MAAP + NIR groups, while other groups exhibited severely disrupted epithelium and substantial infiltration of inflammatory cells. Furthermore, Masson's trichrome staining revealed the presence of hair follicles and more organized collagen fiber alignment in the MAAP + NIR group, indicative of active tissue regeneration and enhanced wound repair.

Bacterial infections often lead to chronic inflammation and delay tissue repair. To assess the immunomodulatory effect of MAAP NSs, macrophage polarization in infected tissues was examined by immunofluorescence staining. As shown in Fig. 6, infected tissues from mice in the MAAP + NIR group displayed the most pronounced CD206 fluorescence and the weakest CD80 fluorescence. These results suggest that macrophage polarized from the pro-inflammatory M1 phenotype to the anti-inflammatory M2 phenotype upon MAAP NS treatment under NIR irradiation. As shown in Fig. S15, after treatment, the levels of the pro-inflammatory cytokine IL-6 significantly decreased at the infection site, while the levels of the angiogenesis marker CD31 significantly increased. These results demonstrate that MAAP NSs can effectively modulate the immune response and promote tissue repair of MRSA-infected wounds in mice.

Given the superior tissue penetration of a NIR-II laser, which has the potential for treating deeper infections, a subcutaneous model of implant-associated MRSA biofilm infection was employed to further evaluate the *in vivo* antibacterial efficacy of MAAP NSs (Fig. 7a). As shown in the infrared thermal images and corresponding temperature curves (Fig. 7b and c), during photothermal therapy (1064 nm, 0.8 W cm^{-2}, 10 min), the skin temperature in the MAAP + NIR group rose rapidly to ~48 °C within 2 min, while the NIR-only group reached only ~35 °C. Throughout the entire treatment period, mouse body weights remained within a reasonable range (Fig. 7d), further indicating the good biocompatibility of MAAP NSs. On day 8 post-treatment, the implants were retrieved to assess biofilm clearance using crystal violet staining and colony counting. As shown in Fig. 7e, substantial biofilms and viable MRSA colonies were observed in the saline and NIR-only groups, whereas the MAAP and MAAP + NIR groups showed marked biofilm

disruption and bactericidal activity. Biofilm biomass quantification (Fig. 7f) revealed a reduction to 52% in the MAAP group and further to 32% in the MAAP + NIR group. Colony counting (Fig. 7g) further confirmed significantly reduced MRSA viability in the MAAP and MAAP + NIR groups, with bacterial inactivation rates of 1.6 log (97%) and 3.1 log (99.92%), respectively.

It is important to assess the retention and clearance of MAAP NSs at treatment sites to ensure long-term safety. We therefore monitored the levels of Au, Ag, and Mo in infected tissues over time. As shown in Fig. S16, the concentrations of Au, Ag, and Mo in infected tissues steadily declined after administration. By the 16th day post-treatment, no metal ions were detectable in the wound tissue, while in *peri*-implant tissues, the levels of Au, Ag, and Mo had decreased by ~89.3%, 90.2%, and 89.4%, respectively. These results indicate that MAAP NSs are progressively cleared through metabolic processes, confirming their biodegradability and excretion capacity and supporting their potential for safe therapeutic use.

4. Conclusions

In summary, MAAP NSs were prepared by sequentially depositing gold and silver nanoparticles onto MoS_2 NSs. Leveraging the plasmonic coupling effect between Au–Ag nanoparticles, MAAP NSs exhibited superior NIR-II photothermal performance and laser-controllable Ag^+ release, establishing them as a novel nano-antibacterial agent with dual antibacterial mechanisms. *In vitro*, under 1064 nm laser irradiation (0.8 W cm^{-2}, 5 min), MAAP NSs inactivated 99.998% of planktonic MRSA and eradicated preformed MRSA biofilms, achieving a 99.992% reduction in biofilm-associated bacteria. *In vivo*, MAAP NSs demonstrated potent antibacterial efficacy by eliminating 99.95% of bacteria in infected wounds under 1064 nm laser irradiation (0.6 W cm^{-2}, 10 min), while simultaneously accelerating wound healing. In a more challenging subcutaneous implant-associated infection model, MAAP NSs effectively disrupted MRSA biofilms on implant surfaces and achieved 99.92% bacterial inactivation under 1064 nm laser irradiation (0.8 W cm^{-2}, 10 min). Considering their simple preparation, excellent antibacterial performance, and good biocompatibility, MAAP NSs are expected to serve as an effective complement to existing clinical infection control strategies and provide valuable insight for the rational design of novel NIR-II laser-responsive antibacterial nanoagents.

Author contributions

L. W. and L. Y. conceived and supervised the project. Q. Z. was responsible for the synthesis, structural characterization, and antibacterial experiments. W. L. and S. Q. contributed to material characterization and data analysis. H. G. and Z. Y. assisted in establishing the animal infection model. W. H. performed the FDTD simulation experiments. Q. Z. and L. Y. co-wrote the initial draft of the manuscript, while L. W. finalized the manuscript and provided conceptual insights. All authors reviewed and approved the final version of the manuscript.

Conflicts of interest

The authors declare no conflicts of interest.

Data availability

The data supporting this article have been included as part of the supplementary information (SI). The SI includes detailed descriptions of the reagents, characterization equipments, and preparation methods, colloidal stability, thermal stability, biosafety, Ag^+ release, inflammation analysis, and metabolism-related data. See DOI: https://doi.org/10.1039/d5nh00627a.

Acknowledgements

This work was financially supported by the National Natural Science Foundation of China (22375101 and 62288102), the Natural Science Foundation of Jiangsu Province-Major Project (BK20212012), and the Belt and Road Innovation Cooperation Project of Jiangsu (BZ2022011).

References

1 T. R. Walsh, A. C. Gales and R. Laxminarayan, *et al.*, Antimicrobial Resistance: Addressing a Global Threat to Humanity, *PLoS Med.*, 2023, **20**(7), e1004264.
2 C. J. L. Murray, K. S. Ikuta and F. Sharara, *et al.*, Global burden of bacterial antimicrobial resistance in 2019: a systematic analysis, *Lancet*, 2022, **399**(10325), 629–655.
3 W. Bank, *Drug-resistant infections: a threat to our economic future*, World Bank, 2017.
4 R. Laxminarayan, T. Van Boeckel and I. Frost, *et al.*, The Commission on antimicrobial resistance: 6 years later, *Lancet Infectious Diseases*, 2020, **20**(4), e51–e60.
5 R. Laxminarayan, A. Duse and C. Wattal, *et al.*, Antibiotic resistance—the need for global solutions, *Lancet Infect. Dis.*, 2013, **13**(12), 1057–1098.
6 E. D. Brown and G. D. Wright, Antibacterial drug discovery in the resistance era, *Nature*, 2016, **529**(7586), 336–343.
7 J. Huo, Q. Jia and H. Huang, *et al.*, Emerging photothermal-derived multimodal synergistic therapy in combating bacterial infections, *Chem. Soc. Rev.*, 2021, **50**(15), 8762–8789.
8 C. Cao, W. Ge and J. Yin, *et al.*, Mesoporous Silica Supported Silver-Bismuth Nanoparticles as Photothermal Agents for Skin Infection Synergistic Antibacterial Therapy, *Small*, 2020, **16**(24), 2000436.
9 L. Chen, X. Sun and K. Cheng, *et al.*, Temperature-regulating phase change fiber scaffold toward mild photothermal–chemotherapy, *Adv. Fiber Mater.*, 2022, **4**(6), 1669–1684.
10 J. Y. Shan, X. Li and K. L. Yang, *et al.*, Efficient Bacteria Killing by Cu_2WS_4 Nanocrystals with Enzyme-like Properties

and Bacteria-Binding Ability, *ACS Nano*, 2019, **13**(12), 13797–13808.
11 W. J. Xiu, L. Wan and K. L. Yang, *et al.*, Potentiating hypoxic microenvironment for antibiotic activation by photodynamic therapy to combat bacterial biofilm infections, *Nat. Commun.*, 2022, **13**(1), 3875.
12 K. L. Yang, C. Shi and Z. W. Yin, *et al.*, Iron metabolism interference-enhanced sonodynamic therapy of methicillin-resistant aureus-induced osteomyelitis by $CaCO_3$-Ga-PPIX@PEG nanospheres, *Nano Today*, 2024, **56**, 102299.
13 C. N. He, P. P. Feng and M. M. Hao, *et al.*, Nanomaterials in Antibacterial Photodynamic Therapy and Antibacterial Sonodynamic Therapy, *Adv. Funct. Mater.*, 2024, **34**(38), 2402588.
14 X. Qi, Y. Xiang and E. Cai, *et al.*, Inorganic–organic hybrid nanomaterials for photothermal antibacterial therapy, *Coord. Chem. Rev.*, 2023, **496**, 215426.
15 Z. J. Qin, Y. K. Zheng and Y. H. Wang, *et al.*, Versatile roles of silver in Ag-based nanoalloys for antibacterial applications, *Coord. Chem. Rev.*, 2021, **449**, 214218.
16 K. Y. Zheng, M. I. Setyawati and D. T. Leong, *et al.*, Antimicrobial silver nanomaterials, *Coord. Chem. Rev.*, 2018, **357**, 1–17.
17 L. Rizzello and P. P. Pompa, Nanosilver-based antibacterial drugs and devices: mechanisms, methodological drawbacks, and guidelines, *Chem. Soc. Rev.*, 2014, **43**(5), 1501–1518.
18 S. Eckhardt, P. S. Brunetto and J. Gagnon, *et al.*, Nanobio Silver: Its Interactions with Peptides and Bacteria, and Its Uses in Medicine, *Chem. Rev.*, 2013, **113**(7), 4708–4754.
19 B. Joseph, V. Sagarika and C. Sabu, *et al.*, Cellulose nanocomposites: Fabrication and biomedical applications, *J. Bioresour. Bioprod.*, 2020, **5**(4), 223–237.
20 N. Lu, Z. Chen and W. Zhang, *et al.*, Effect of silver ion implantation on antibacterial ability of polyethylene food packing films, *Food Packag. Shelf Life*, 2021, **28**, 100650.
21 L. Wang, G. Periyasami and A. Aldalbahi, *et al.*, The antimicrobial activity of silver nanoparticles biocomposite films depends on the silver ions release behaviour, *Food Chem.*, 2021, **359**, 129859.
22 B. Le Ouay and F. Stellacci, Antibacterial activity of silver nanoparticles: a surface science insight, *Nano Today*, 2015, **10**(3), 339–354.
23 L. M. Stabryla, K. A. Johnston and N. A. Diemler, *et al.*, Role of bacterial motility in differential resistance mechanisms of silver nanoparticles and silver ions, *Nat. Nanotechnol.*, 2021, **16**(9), 996–1003.
24 Y. Qiao, J. He and W. Y. Chen, *et al.*, Light-Activatable Synergistic Therapy of Drug-Resistant Bacteria-Infected Cutaneous Chronic Wounds and Nonhealing Keratitis by Cupriferous Hollow Nanoshells, *ACS Nano*, 2020, **14**(3), 3299–3315.
25 X. S. Zhao, H. Y. Qiu and Y. Shao, *et al.*, Silver Nanoparticle-Modified 2D MOF Nanosheets for Photothermally Enhanced Silver Ion Release Antibacterial Treatment, *Acta Phys.-Chim. Sin.*, 2023, **39**(7), 2211043.
26 L. H. Yuwen, Y. T. Sun and G. L. Tan, *et al.*, MoS_2@polydopamine-Ag nanosheets with enhanced antibacterial activity for effective treatment of Staphylococcus aureus biofilms and wound infection, *Nanoscale*, 2018, **10**(35), 16711–16720.
27 X. Nie, S. Wu and F. Huang, *et al.*, ''Dew-of-Leaf'' structure multiple synergetic antimicrobial modality hybrid: a rapid and long lasting bactericidal material, *Chem. Eng. J.*, 2021, **416**, 129072.
28 M. Zhu, X. M. Liu and L. Tan, *et al.*, Photo-responsive chitosan/Ag/MoS_2 for rapid bacteria-killing, *J. Hazard. Mater.*, 2020, **383**, 121122.
29 S. Suran, N. Kamyar and K. Huang, *et al.*, Tunable Release of Ions from Graphene Oxide Laminates for Sustained Antibacterial Activity in a Biomimetic Environment, *Small*, 2024, **21**(28), 2304850.
30 C. Fu, Y. Fan and G. Liu, *et al.*, One-step fabrication of an injectable antibacterial collagen hydrogel with in situ synthesized silver nanoparticles for accelerated diabetic wound healing, *Chem. Eng. J.*, 2024, **480**, 148288.
31 Q. M. Hong, W. Zhang and Z. Liu, *et al.*, Infection microenvironment-triggered nanoparticles eradicate MRSA by thermally amplified chemodynamic therapy and M1 macrophage, *J. Nanobiotechnol.*, 2024, **22**(1), 448.
32 H. Li, M. Gong and J. Xiao, *et al.*, Photothermally activated multifunctional MoS_2 bactericidal nanoplatform for combined chemo/photothermal/photodynamic triple-mode therapy of bacterial and biofilm infections, *Chem. Eng. J.*, 2022, **429**, 132600.
33 Y. Xu, C. Li and J. An, *et al.*, Construction of a 980 nm laser-activated Pt(II) metallacycle nanosystem for efficient and safe photo-induced bacteria sterilization, *Sci. China Chem.*, 2023, **66**(1), 155–163.
34 B. Guo, Z. Feng and D. Hu, *et al.*, Precise deciphering of brain vasculatures and microscopic tumors with dual NIR-II fluorescence and photoacoustic imaging, *Adv. Mater.*, 2019, **31**(30), 1902504.
35 Z. Mei, D. Gao and D. Hu, *et al.*, Activatable NIR-II photoacoustic imaging and photochemical synergistic therapy of MRSA infections using miniature Au/Ag nanorods, *Biomaterials*, 2020, **251**, 120092.
36 W. Zhang, K. Cai and Z. Sun, *et al.*, Elevating second near-infrared photothermal conversion efficiency of hollow gold nanorod for a precise theranostic of orthotopic bladder cancer, *ACS Nano*, 2023, **17**(19), 18932–18941.
37 J. He, S. Hua and D. Zhang, *et al.*, SERS/NIR-II Optical Nanoprobes for Multidimensional Tumor Imaging from Living Subjects, Pathology, and Single Cells and Guided NIR-II Photothermal Therapy, *Adv. Funct. Mater.*, 2022, **32**(46), 2208028.
38 C. Bi, J. Chen and Y. Chen, *et al.*, Realizing a Record Photothermal Conversion Efficiency of Spiky Gold Nanoparticles in the Second Near-Infrared Window by Structure-Based Rational Design, *Chem. Mater.*, 2018, **30**(8), 2709–2718.
39 Z. W. Li, W. S. Wang and Y. D. Yin, Colloidal Assembly and Active Tuning of Coupled Plasmonic Nanospheres, *Trends Chem.*, 2020, **2**(7), 593–608.

40 Q. R. Fu, Z. Li and F. F. Fu, *et al.*, Stimuli-Responsive Plasmonic Assemblies and Their Biomedical Applications, *Nano Today*, 2021, **36**, 101014.
41 X. J. Cheng, R. Sun and L. Yin, *et al.*, Light-Triggered Assembly of Gold Nanoparticles for Photothermal Therapy and Photoacoustic Imaging of Tumors In Vivo, *Adv. Mater.*, 2017, **29**(6), 1604894.
42 F. Chen, Y. Luo and X. Liu, *et al.*, 2D Molybdenum Sulfide-Based Materials for Photo-Excited Antibacterial Application, *Adv. Healthcare Mater.*, 2022, **11**(13), 2200360.
43 L. H. Yuwen, H. Yu and X. R. Yang, *et al.*, Rapid preparation of single-layer transition metal dichalcogenide nanosheets via ultrasonication enhanced lithium intercalation, *Chem. Commun.*, 2016, **52**(3), 529–532.
44 R. Dai, A. Zhang and Z. Pan, *et al.*, Epitaxial Growth of Lattice-Mismatched Core–Shell TiO_2@MoS_2 for Enhanced Lithium-Ion Storage, *Small*, 2016, **12**(20), 2792–2799.
45 L. Yuwen, F. Xu and B. Xue, *et al.*, General synthesis of noble metal (Au, Ag, Pd, Pt) nanocrystal modified MoS_2 nanosheets and the enhanced catalytic activity of Pd-MoS_2 for methanol oxidation, *Nanoscale*, 2014, **6**(11), 5762–5769.
46 T. Ishida, T. Murayama and A. Taketoshi, *et al.*, Importance of size and contact structure of gold nanoparticles for the genesis of unique catalytic processes, *Chem. Rev.*, 2019, **120**(2), 464–525.
47 H. Mao, Y. Fu and H. Yang, *et al.*, Structure-activity relationship toward electrocatalytic nitrogen reduction of MoS_2 growing on polypyrrole/graphene oxide affected by pyridinium-type ionic liquids, *Chem. Eng. J.*, 2021, **425**, 131769.
48 Y. Xu, S. Duan and H. Li, *et al.*, Au/$Ni_{12}P_5$ core/shell single-crystal nanoparticles as oxygen evolution reaction catalyst, *Nano Res.*, 2017, **10**(9), 3103–3112.
49 J. Xu, J. Hu and C. Peng, *et al.*, A simple approach to the synthesis of silver nanowires by hydrothermal process in the presence of gemini surfactant, *J. Colloid Interface Sci.*, 2006, **298**(2), 689–693.
50 Y. Zhang, W. Xiu and Y. Sun, *et al.*, RGD-QD-MoS_2 nanosheets for targeted fluorescent imaging and photothermal therapy of cancer, *Nanoscale*, 2017, **9**(41), 15835–15845.
51 S. J. Kim, W.-K. Ko and D. N. Heo, *et al.*, Anti-neuroinflammatory gold nanocomplex loading ursodeoxycholic acid following spinal cord injury, *Chem. Eng. J.*, 2019, **375**, 122088.
52 P. Li, Z. Chen and F. Xia, *et al.*, Leveraging Coupling Effect-Enhanced Surface Plasmon Resonance of Ruthenium Nanocrystal-Decorated Mesoporous Silica Nanoparticles for Boosted Photothermal Immunotherapy, *Adv. Healthcare Mater.*, 2023, **12**(31), e2302111.
53 J. Liu and R. H. Hurt, Ion Release Kinetics and Particle Persistence in Aqueous Nano-Silver Colloids, *Environ. Sci. Technol.*, 2010, **44**(6), 2169–2175.
54 Y. Cheng, Y. Zhang and Z. Zhao, *et al.*, Guanidinium-Decorated Nanostructure for Precision Sonodynamic-Catalytic Therapy of MRSA-Infected Osteomyelitis, *Adv. Mater.*, 2022, **34**(50), 2206646.
55 A. Sousa, A. N. Phung and N. Škalko-Basnet, *et al.*, Smart delivery systems for microbial biofilm therapy: dissecting design, drug release and toxicological features, *J. Controlled Release*, 2023, **354**, 394–416.
56 J. A. O'Donnell, M. Wu and N. H. Cochrane, *et al.*, Efficacy of common antiseptic solutions against clinically relevant microorganisms in biofilm, *Bone Joint J.*, 2021, **103-B**(5), 908–915.
57 M. K. Luther, D. M. Parente and A. R. Caffrey, *et al.*, Clinical and Genetic Risk Factors for Biofilm-Forming Staphylococcus aureus, *Antimicrob. Agents Chemother.*, 2018, **62**(5), e02252–02217.

